JMEPEG (2010) 19:452–466
DOI: 10.1007/s11665-010-9610-8

Finite Element Prediction of Creep-Plastic Ratchetting and Low Cycle Creep-Fatigue for a Large SPF Tool

A.A. Deshpande, S.B. Leen, and T.H. Hyde

(Submitted December 9, 2009)

Industrial experience shows that large superplastic forming (SPF) tools suffer from distortion due to thermal cycling, which apparently causes high temperature creep and plasticity. In addition to distortion, thermomechanical fatigue and fatigue-creep interaction can lead to cracking. The aim of this study is to predict the life-limiting thermomechanical behavior of a large SPF tool under realistic forming conditions using elastic-plastic-creep FE analyses. Nonlinear time-dependent, sequentially coupled FE analyses are performed using temperature-dependent monotonic and cyclic material data for a high-nickel, high-chromium tool material, XN40F (40% Ni and 20% Cr). The effect of monotonic and cyclic material data is compared vis-à-vis the anisothermal, elastic-plastic-stress response of the SPF tool. An uncoupled cyclic plasticity-creep material model is employed. Progressive deformation (ratchetting) is predicted locally, transverse to the predominant direction of the creep-fatigue cycling, but at the same spatial location, due to creep and cyclic plasticity, during the so-called minor cycles, which correspond to comparatively small-amplitude temperature changes associated with opening of the press doors during part loading and unloading operations.

Keywords creep ratchetting, heating-cooling cycles, major cycle, minor cycle, part-forming cycles, plastic shakedown, superplastic forming, thermomechanical fatigue and creep

1. Introduction

Superplastic forming is an important manufacturing process for the aerospace and the automotive industries because of its capability of producing highly complex sheet components in a single operation. The SPF process is generally used to form complex geometry-shaped components and requires complex-shaped tools. Tools play an important role in the success of any manufacturing process. Superplastic forming tools need to withstand high temperature cyclic loading and steady mechanical loading for extended durations and, therefore, are manufactured (by casting) from specialized alloys, but at the same time, numerous additional geometrical complexities result from weight-saving constraints (due, for example, to weight limitations in industrial plant related to, for example, handling capacities) and ruling section requirements for casting. The cost of tool failure is significant, and tool life is an important limiting aspect in the SPF process; the SPF process is a high value-added process, rather than a mass production process.

Comparatively little research has been carried out in the area of thermomechanical analysis of SPF tools. The group of Bernhart and co-workers (Ref 1, 2) at Ecoles des Mines at Albi have presented thermomechanical finite element (FE) analyses of a simple axisymmetric, cylindrical-shaped SPF tool and investigated the effects of residual stress and distortion. A steady-state heat transfer analysis was employed with thermal gradients, using non-isothermal boundary conditions, to drive thermomechanical FE analysis with elastic-viscoplastic material behavior during the forming cycle. The thermomechanical fatigue properties were measured through thermomechanical fatigue tests, and a complex unified elastic-viscoplastic material model has been developed for forging and SPF tool materials. Shang et al. (Ref 3-5) have studied the thermomechanical, time-dependent, elastic-plastic, and creep behavior of large SPF tools using a sequential, three-dimensional, FE heat transfer and mechanical stress analysis approach. In the absence of sufficient test data, the measured temperature-dependent monotonic stress-strain data were employed to define an anisothermal, linear kinematic hardening model. Shang et al. (Ref 4) characterized high temperature behavior of the 40%Ni-20%Cr, XN40F tool material using isothermal fatigue and creep-fatigue interaction tests at 700 and 900 °C. A creep-fatigue life prediction method using a novel bilinear strain-range partitioning approach was developed and applied to predict the tool life. Shang et al. (Ref 3) used simplified boundary conditions, i.e., contact with the platen was not modeled, and the effects of clamping pressure during the forming cycle were not considered.

Large SPF tools mainly suffer from distortion due to thermal cycling and high temperature creep. Creep relaxation during

---

This article is based on a presentation at the AeroMat Conference, International Symposium on Superplasticity and Superplastic Forming (SPF) held in Austin, TX, June 23-26, 2008.

A.A. Deshpande and **T.H. Hyde**, Division of Materials, Mechanics and Structures, University of Nottingham, Nottingham NG7 2RD, UK; and **S.B. Leen**, Mechanical and Biomedical Engineering, College of Engineering and Informatics, National University of Ireland, Galway, Ireland. Contact e-mails: aditya.deshpande@nottingham.ac.uk, sean.leen@nuigalway.ie, and thomas.hyde@nottingham.ac.uk.

forming induces inelastic deformation and distortion of the tool after cooling to the ambient (Ref 2). SPF tool distortion can lead to the forming of inaccurate parts, which incurs the expensive repair and replacement of such tools. In addition to distortion, the thermomechanical fatigue and fatigue-creep interaction can lead to cracking. Finite element (FE)-based simulation of realistic thermomechanical conditions is an effective (arguably the only full-field) method for analyzing realistic large SPF tool behavior to predict the complex temperature-stress-strain cycles and hence damage and deformation for distortion assessment and hence distortion control or minimization.

All engineering structures subjected to cyclic loading above the first yield load of the structure may fail due to different mechanisms such as elastic shakedown, plastic shakedown, or ratchetting. In elastic shakedown, a structure shakes down to elastic behavior after an initial elastic-plastic response and may fail after a finite number of cycles due to high cycle fatigue. Structure behavior exhibiting stable reverse or alternating plasticity over each cycle is referred to as plastic shakedown. In plastic shakedown, the structure can be expected to fail due to low cycle fatigue. Alternatively, structural behavior exhibiting an accumulation of (plastic) strain with each loading cycle is referred to as ratchetting due to which incremental plastic collapse or failure of the structure will occur. At high temperature, the viscosity of the material and the time dependence of ratchetting become important and should be addressed for the safety of components (Ref 6).

This article is concerned with the FE prediction of the complex aniosthermal, time-dependent, thermomechanical behavior of realistic SPF tools, under complex thermomechanical load cycles, corresponding to (i) low-frequency bulk heating and cooling of the tool and (ii) higher-frequency localized cooling and heating of the tool, associated with blank insertion and part removal. This study is relevant to real industrial problems with distortion of such tools, leading to detrimental cracking and tool repair/refurbishement overheads and associated outage. The predictions suggest that SPF tools experience low cycle fatigue, creep-fatigue, and high temperature creep-plastic ratchetting, and that the so-called minor cycles, corresponding to localized cooling and heating of the tools due to press opening for blank insertion and part removal, are particularly detrimental with respect to damage accumulation. In the absence of sufficient test data, initially temperature-dependent monotonic stress-strain data are used to define a cyclic stress-strain curve. Following Kapoor (Ref 7), who considered ratcheting and fatigue to be independent but competing mechanisms, estimated predictions are provided for the ratchetting and creep-fatigue lives of the tool to assess their comparative importance.

2. Tool Geometry and Material

The geometry of a realistic SPF tool is shown in Fig. 1. Side A is approximately 2000 mm long, and side B is approximately 800 mm long. The bottom side of the tool has eleven cavities of 100-mm depth, for casting purposes. Figure 1 also shows the forming surface of the tool and other features such as alignment lugs and hangers.

In practice, major cracks are typically observed along the top edges of the two longer sides shown in Fig. 1 while smaller cracks tend to occur at stress concentration features, such as alignment lugs, hangings, and corner cavities.

The tool is cast from XN40F material which is relatively new in the aerospace industry. The composition of XN40F tool material is given in Table 1 (Ref 5) while the thermal properties are given in Table 2 (Ref 5). Thermal properties such as thermal conductivity and specific heat at different temperatures are required to predict the thermal histories of the SPF tool.

The material data from high temperature tensile tests and cyclic isothermal tests from previous study at the University of Nottingham (Ref 5), along with new data presented here, are shown in Table 3-5. The tensile tests were carried out for four different temperatures; 20, 500, 700, and 900 °C which span the temperature range for the SPF process. The average strain rate applied is 8×10^{-4} s^{-1}. Figure 2 and Table 3 show the results of monotonic tension tests. The elongation to failure increases significantly with increasing temperature. Brittle fracture occurs below 700 °C, and ductile fracture occurs at 900 °C (Ref 5). Short-term tensile tests at lower strain rates of

Table 1 Composition of the SPF tool material XN40F (Ref 5)

Elements	C	Ni	Cr	Fe
wt.%	0.35	40.0	20.0	Balance

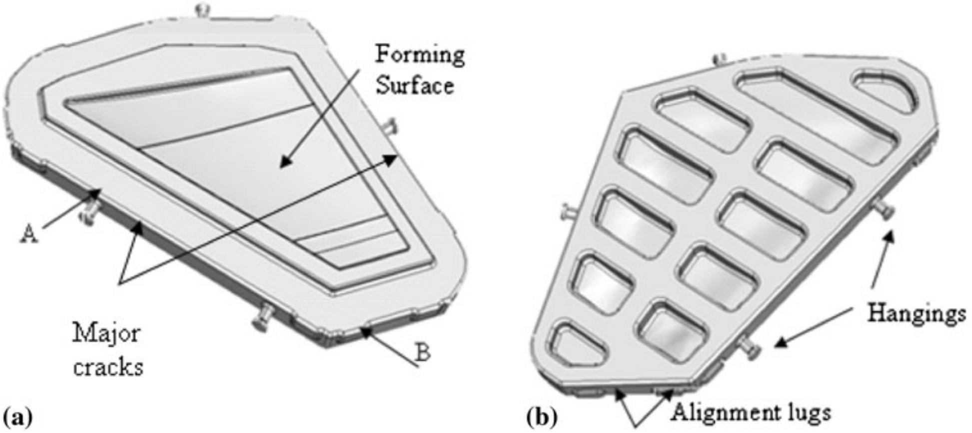

Fig. 1 Geometry of realistic superplastic forming tool: (a) top view SPF tool; (b) bottom view of SPF tool

Table 2 Thermal properties of XN40F material at different temperatures (after Ref 5)

Thermal conductivity λ		Thermal expansion α		Specific heat c_p	
Temperature, °C	W/m/K	Temperature, °C	$\times 10^{-6}$/°C	Temperature, °C	J/kg/K
20	11	20-100		0	437
500	20	20-500	15.8	500	536
850	26	20-850	17.35	850	603
950	28	20-950	17.7	950	618

Table 3 Measured mechanical properties of XN40F material at different temperatures of strain rate 8×10^{-4} s^{-1} (Ref 5)

Temperature, °C	Young's modulus, GPa	0.2% Yield strength, MPa	UTS, MPa	Elongation, %	$C = \frac{\partial\sigma}{\partial\varepsilon^{pl}}$, MPa
20	110	172	332	3	6154
500	108	145	320	6	3182
700	104	110	286	16	1213
900	92	107	120	37	36

Table 4 Measured creep properties of XN40F material of 900 °C (Ref 5)

Strain rates, s^{-1}	Stress, MPa	A, MPa^{-n} s^{-1}	n
8×10^{-4}	136	9.14×10^{-14}	4.66
8×10^{-5}	83		

Table 5 Measured mechanical properties of XN40F material at different temperatures from strain-controlled cyclic tests (Ref 5 and this study)

Temperature, °C	Young's modulus, GPa	Yield strength, MPa	Peak stress, MPa	$C = \frac{\partial\sigma}{\partial\varepsilon^{pl}}$, MPa
20	110	238	292	16363
500	108	180	292	33939
700	104	175	295	10619
900	92	112	186	6352

8×10^{-5} and 8×10^{-4} s^{-1} at 900 °C were carried out to determine the short-term creep properties as shown in Table 4 and Fig. 3.

Cyclic isothermal tests at 20, 500, 700, and 900 °C for different strain ranges were employed to characterize the temperature-dependent cyclic stress-strain behavior of the XN40F alloy. Lower strain-ranges were employed for the lower temperatures, consistent with anticipated relevant in situ conditions. Figure 4 shows the cyclic stress-strain curves obtained from the tests for different temperatures. It can be seen that the alloy cyclically hardens at all temperature. The degree of hardening is greater at lower temperatures than at higher temperatures. The lowest hardening observed was at 900 °C.

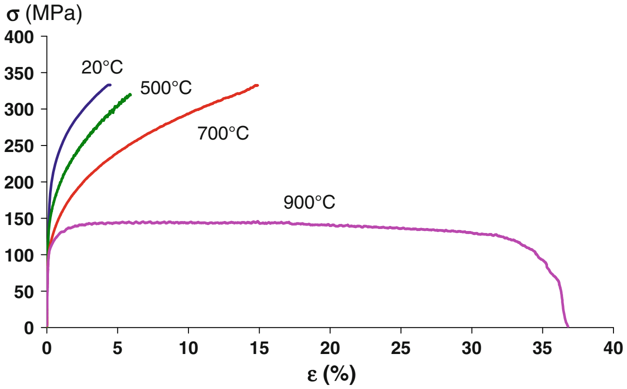

Fig. 2 Tensile test stress-strain curves at different temperatures (20, 500, 700, and 900 °C) for strain rate of 8×10^{-4} s^{-1} (Ref 5)

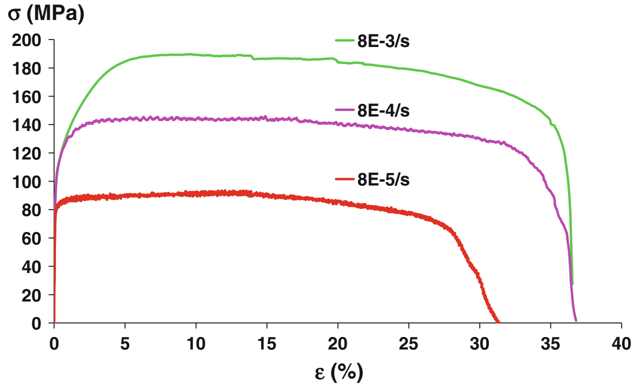

Fig. 3 Stress-strain curves of 900 °C tensile tests at different strain rates (Ref 5)

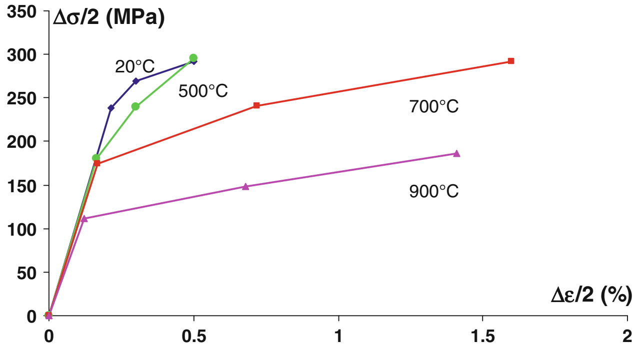

Fig. 4 Cyclic test stress-strain curves at different temperatures (20, 500, 700 and 900 °C) for strain rate of 8×10^{-4} s^{-1}

3. Methodology

3.1 General

The realistic SPF tool shown in Fig. 1 is represented in a geometrically simplified form (see Fig. 5) to reduce the computational expense and complexities in the FE model. The main simplifications relate to the omission of local features, such as hangings and alignment lugs, so that the dominant deformation mechanisms are still captured, since the

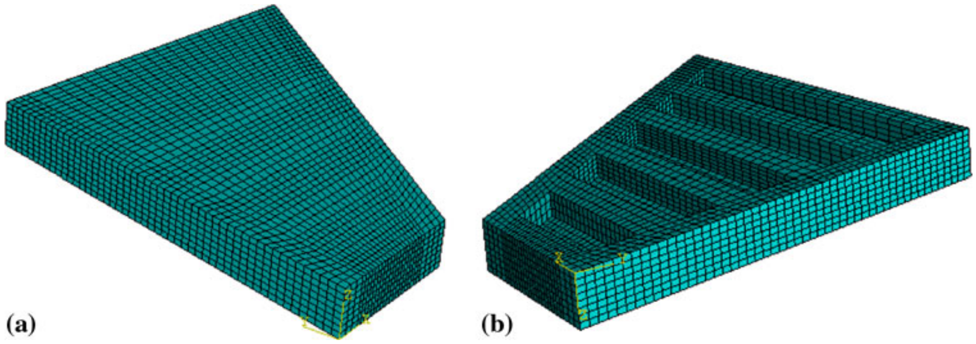

Fig. 5 The FE model of a half of a simplified SPF tool: (a) top view, (b) bottom view

objective here is to address the major cracks observed in real tools. A lower half of the SPF tool is modeled assuming symmetry between the upper and lower tool. The platen-tool contact is defined as a mechanical boundary condition in the FE model. This representative tool has five cavities of 100-mm depth on the underside of the tool.

The transient heat transfer methodology used here is the same as that previously validated against the measured heating and cooling experiments for a model tool at the University of Nottingham (Ref 4). A realistic SPF thermal history is modeled in the commercial, general-purpose, non-linear FE code, ABAQUS, using conduction, convection, and radiation mechanisms.

3.2 Heat Transfer modeling

Thermal conductivity is a thermophysical property of material which is a function of temperature and location, i.e., $k = k(T, x, y, z)$ (Ref 8). In this study, since the tool is assumed to be homogeneous and isotropic, it is assumed that $k = k(T)$ only. The temperature-dependent conductivity data from Table 2 illustrates the FE modeling of the SPF thermal cycles.

Newton's law of cooling which gives the relation between convective heat transfer rate and temperature difference between the surface T_s and ambient T_∞ is used to model convective heat transfer (Ref 8), as follows:

$$q'' = h(T_s - T_\infty) \qquad \text{(Eq 1)}$$

where h is the convective heat transfer coefficient and q'' is the convective heat flux. SPF tools are commonly (or at least partially) cooled with a natural flow of air, so that the natural convection mechanism is assumed for calculating convective heat transfer coefficients.

Convective heat transfer coefficients are commonly expressed using the Nusselt non-dimensional number which is defined as

$$Nu_L = \frac{hL}{k} = CRa_L^n \qquad \text{(Eq 2)}$$

where L is the characteristic length of the geometry, k is the conductivity of air, and Ra_L is the Rayleigh number, given by

$$Ra_L = \frac{g\beta(T_s - T_\infty)}{v\alpha} \qquad \text{(Eq 3)}$$

where g is the local acceleration due to gravity, β is the volumetric thermal expansion coefficient, defined as $\beta = \frac{1}{T}$ for an ideal gas, v is kinematic viscosity (m^2/s), and α is thermal diffusivity (m^2/s). The convective heat transfer coefficient changes depending on the surface orientation.

For a vertical surface, which is parallel with the gravitational vector; the buoyancy force causes fluid motion in the upward or downward direction, and the following empirical formula is used to calculate h for vertical surfaces (Ref 8):

$$\overline{Nu_L} = 0.68 + \frac{0.670 Ra_L^{1/4}}{[1 + (0.492\alpha/v)^{9/16}]^{4/9}} \quad Ra_L \le 10^9 \qquad \text{(Eq 4)}$$

Alternatively, for a horizontal surface, the buoyancy force is normal to the surface and the recommended correlations (Ref 8) for the average Nusselt number are given as follows:

(a) For the upper surface of a heated plate or the lower surface of cooled plate:

$$\overline{Nu_L} = 0.54 Ra_L^{1/4} \quad (10^4 \le Ra_L \le 10^7) \qquad \text{(Eq 5)}$$

$$\overline{Nu_L} = 0.15 Ra_L^{1/3} \quad (10^7 \le Ra_L \le 10^{11}) \qquad \text{(Eq 6)}$$

(b) For the lower surface of a heated plate or the upper surface of cooled plate:

$$\overline{Nu_L} = 0.27 Ra_L^{1/4} \quad (10^5 \le Ra_L \le 10^{10}) \qquad \text{(Eq 7)}$$

These equations are employed to calculate the film coefficients for modeling of convective heat transfer of the SPF tool.

The ratio of radiation emitted by a surface to the radiation emitted by a black body is called the emissivity (Ref 8). The emissivity of a black body is assumed to equal 1, and no surface can emit more radiation than a black body. The radiative heat transfer is defined here via the following equation:

$$q = eC_{SB}T^4 \qquad \text{(Eq 8)}$$

where e is the radiation emissivity of the surface, q is the surface emissive power (W/m^2), T is the absolute temperature of the surface, and C_{SB} is the Stefan-Boltzmann constant, which is equal to $C_{SB} = 5.67 \times 10^{-8}$ W/m^2 K.

Previous calibration of the present heat transfer methodology against the measured transient temperature history of a representative tool has shown that a value of $e = 0.9$ is appropriate for accurate prediction of the cooling and heating cycles.

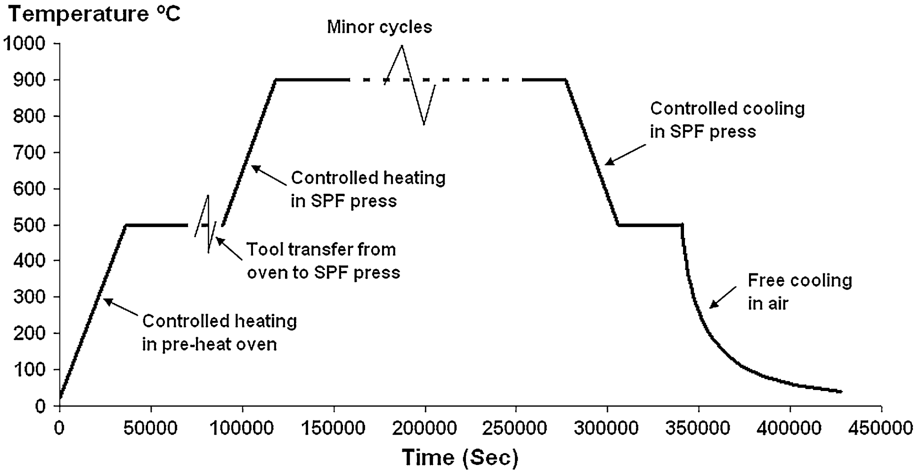

Fig. 6 Specified major cycle temperature history of the SPF tool

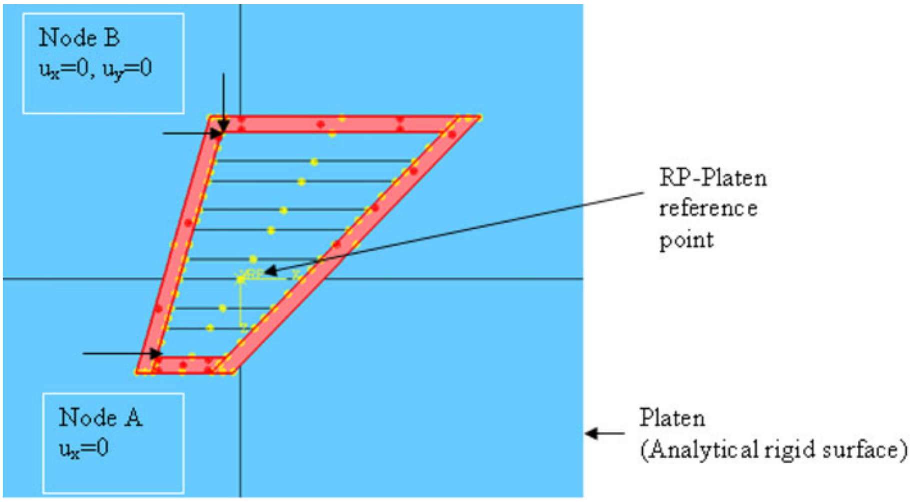

Fig. 7 Mechanical boundary conditions and clamping pressure for FE model of SPF tool and platen

3.3 SPF Thermal Cycle

The SPF tool temperature cycling is complex and is therefore idealized here as divided into two types. The two types are (i) lower frequency cycles, referred here as major cycles, broadly associated with heating and cooling from ambient, and (ii) higher frequency cycles, referred to here as minor cycles, which are associated with opening and closing of the press doors for blank inserts and removal of formed parts. In reality, these cycles are not easy to standardize since they are not automated and are carried out by manual operation. Therefore, there can be significant variations in the time periods, in particular, associated with these idealized cycles. Nonetheless, for the purposes of analyses here, they are idealized as follows.

3.3.1 Major Cycle.

Step 1: The tool is heated in a pre-heat furnace to 500 °C at a controlled rate of 50 °C/h and then allowed to reach steady state by soaking at 500 °C. The heating process is mainly controlled by conduction with the temperature boundary condition applied to the bottom surface of the tool. The open radiation and free convection mechanisms are also applied with an ambient temperature of 500 °C during the soak time.

Step 2: The tool is transferred to the SPF press in 3 min. During this time period, all external surfaces except the top surface of the tool are exposed to the ambient via open radiation and free convection mechanisms.

Step 3: The tool arrives in the SPF press and is heated to 900 °C, again at 50 °C/h, until a uniform temperature is achieved. This process is again controlled through the conductive heating of the tool via temperature control of the bottom surface nodes.

Step 4: The tool is control-cooled to 500 °C at 50 °C/h in the SPF press and then removed from the press to cool to ambient temperature via free convection and open radiation.

These four (major cycle) steps are illustrated in Fig. 6. Direct heating and cooling to 500 °C in the SPF press is always implemented by controlled temperature variation of the tool bottom surface nodes. The contact with the platen is assumed to be adiabatic (Fig. 7).

3.3.2 Minor Cycle.

Step 1: The SPF press is opened to unload the formed component. This consists of allowing the two longest sides of the tool (facing the press doors) to cool via free convection and open radiation with the ambient for a period of 5 min.

Step 2: The press is closed again, and the tool is heated back to 900 °C.

Step 3: The press is opened again to load the new blank. This again allows the two longest sides to cool via free convection and open radiation for 5 min.

Step 4: The press is closed again, and the tool is heated back to 900 °C along with the new blank sheet.

Step 5: The tool and the blank temperature is maintained at a constant temperature of 900 °C for 7 h corresponding to the forming cycle of one component.

3.4 Constitutive Equations

The material constitutive model employed here is a temperature-dependent, linear, kinematic-hardening (LKH) model, with uncoupled secondary (Norton) creep during the dwell time at 900 °C. The Ziegler kinematic-hardening law within ABAQUS (Ref 9) is used to simulate the translation of yield surface in the stress space, through the back stress, $\boldsymbol{\alpha}$.

The total strain rate is decomposed into elastic and plastic strain rates, as follows:

$$\dot{\boldsymbol{\varepsilon}} = \dot{\boldsymbol{\varepsilon}}^{\mathrm{el}} + \dot{\boldsymbol{\varepsilon}}^{\mathrm{pl}} \qquad \text{(Eq 9)}$$

with the linear elastic behavior defined as

$$\boldsymbol{\sigma} = \mathbf{D}^{\mathrm{el}}:\boldsymbol{\varepsilon} \qquad \text{(Eq 10)}$$

where $\mathbf{D}^{\mathrm{el}}$ is the material stiffness matrix and the yield surface is defined by

$$f(\boldsymbol{\sigma} - \boldsymbol{\alpha}) = \sigma^0 \qquad \text{(Eq 11)}$$

where σ^0 is the size of the yield surface and $f(\boldsymbol{\sigma} - \boldsymbol{\alpha})$ is the equivalent Mises stress with respect to the back stress $\boldsymbol{\alpha}$ defined as

$$f(\boldsymbol{\sigma} - \boldsymbol{\alpha}) = \sqrt{\frac{3}{2}(\mathbf{S} - \boldsymbol{\alpha}^{\mathrm{dev}}):(\mathbf{S} - \boldsymbol{\alpha}^{\mathrm{dev}})} \qquad \text{(Eq 12)}$$

where $\boldsymbol{\alpha}^{\mathrm{dev}}$ is the deviatoric part of the back stress and $\mathbf{S}$ is the deviatoric stress tensor. The flow-rule equation is

$$\dot{\boldsymbol{\varepsilon}}^{\mathrm{pl}} = \frac{\partial f(\boldsymbol{\sigma} - \boldsymbol{\alpha})}{\partial \boldsymbol{\sigma}} \dot{\bar{\varepsilon}}^{\mathrm{pl}} \qquad \text{(Eq 13)}$$

where $\dot{\bar{\varepsilon}}^{\mathrm{pl}}$ is the equivalent plastic strain rate defined as follows:

$$\dot{\bar{\varepsilon}}^{\mathrm{pl}} = \sqrt{\frac{2}{3}\dot{\boldsymbol{\varepsilon}}^{\mathrm{pl}}:\dot{\boldsymbol{\varepsilon}}^{\mathrm{pl}}} \qquad \text{(Eq 14)}$$

The size of the yield surface $\sigma^0(T)$ is a function of temperature T and the generalized Ziegler's rule for an-isothermal case is given in equation below:

$$\dot{\boldsymbol{\alpha}} = C\dot{\bar{\varepsilon}}^{\mathrm{pl}} \frac{1}{\sigma^0}(\boldsymbol{\sigma} - \boldsymbol{\alpha}) + \frac{1}{C}\boldsymbol{\alpha}\dot{C} \qquad \text{(Eq 15)}$$

where $C(T)$ is the temperature-dependent hardening modulus of the isothermal uni-axial stress-strain response, $\frac{\partial \boldsymbol{\sigma}}{\partial \bar{\varepsilon}^{\mathrm{pl}}}$, measured at different temperatures and $\dot{C}$ is the rate of change of C with respect to temperature, as given in Table 3 and 5, for the monotonic and cyclic data, respectively.

A steady-state (secondary) creep behavior is introduced during the (minor cycle) dwell time at the constant temperature of 900 °C. Creep is applied in the model using power-law (Norton) creep $\dot{\bar{\varepsilon}}^{\mathrm{cr}} = Aq^n t^m$ where A, n and m are temperature-dependent material constants, $\dot{\bar{\varepsilon}}^{\mathrm{cr}}$ is the uniaxial equivalent creep strain rate, q is the equivalent (von Mises) stress, and t is the total time. A value of $m = 0$ is assumed here, so that only secondary creep is considered.

3.5 Finite Element modeling

Sequentially coupled thermomechanical analyses are performed to simulate the thermomechanical behavior of the SPF tool. The time-dependent temperature distribution from the transient heat transfer phase is employed in a subsequent thermomechanical analysis, where thermal stresses and strains are calculated using temperature-dependent thermal expansion coefficients. As mentioned above, only the lower half of the tool is modeled, as a first approximation and on the basis of approximate symmetry between the two halves. The presence of upper tool is modeled via the clamping pressure applied along the top edge of the lower tool during the dwell time. The gas pressure during forming is not modeled as the stresses induced by the forming pressure are considered to be negligible (Ref 2). Tool gravity is modeled along with frictional contact between the tool bottom surface and platen.

In FE analysis, contact is classified as a discontinuous constraint which allows forces to be transmitted from one part to another. The constraint is only applied when the two surfaces are in contact, and hence the analysis has to be able to detect when the two surfaces are in contact and apply the constraint accordingly. Contact problems are difficult to converge and must be addressed properly.

The contact between the two surfaces is defined using the slave-master algorithm in ABAQUS. The platen is defined as an analytically rigid surface and is assigned to be the master surface. The bottom surface of the tool is defined as a slave surface. The platen (master surface) is extended enough well beyond the bottom surface (slave) of the tool to avoid slave surface nodes "falling off the edge" of the master surface. Interaction between contacting surfaces consist of normal and tangential components. When two surfaces are in contact with each other, the force normal to the contacting surfaces acts on the two bodies. The surfaces separate when contact pressure between them becomes zero or negative, and the constraint is removed. This surface interaction is referred to as hard contact (Ref 9) and is used to model the normal behavior between the platen and the tool. In the presence of friction, shear forces are created between the contacting surfaces, which resist the tangential motion of the bodies. The Coulomb friction model is used here to describe this interaction between the platen and the tool. The frictional behavior is defined using a coefficient of friction μ which is equal to 0.2 in the tool-platen contact. Contact with friction is difficult to converge due to the discontinuity between the two states of sticking or slipping. A penalty friction formulation with an allowable elastic slip is employed here. The allowable elastic slip is the small amount of relative motion that occurs when surfaces should be under sticking state which corresponds to a very small fraction of the characteristic element length (Ref 9). An allowable elastic slip value of 0.2 mm is used here.

First-order elements are always preferred for slave surfaces over second-order elements (Ref 9) and hence eight-noded (linear) brick elements with reduced integration are used in the thermomechanical analyses. The ABAQUS algorithm always checks for changes in the contact conditions (closed or opened) before checking for equilibrium forces and moments. Iterations with contact state changes detected are called severe discontinuity iterations. In order to converge contact successfully, the maximum number of severe discontinuity equations allowed are changed from default 12-30 in the current problem, and the contact is converged successfully.

A reference point on the platen is constrained in all six degrees of freedom throughout the analyses. Boundary conditions are applied at nodes A and B (Fig. 7) in the beginning of the analysis to restrict tool rotation across the horizontal plane until the friction between the platen and the tool bottom surface is completely active i.e., only during the application of gravity of the tool.

The SPF tool is subjected to three different types of loading during the SPF process, namely, thermal-mechanical loading, gravity loading, and clamping pressure. Tool gravity is applied at the beginning of the analyses and remains active throughout. The clamping pressure of 4 MPa is applied along the top surface edges of the SPF tool just before the forming cycle and remains active during the 7-h forming period. The clamping pressure in real tools is commonly actively controlled, both spatially and temporally, but this aspect is not modeled here.

3.6 Tool Life Prediction Methodology

It is well known that some materials, such as stainless steel 304, do not follow a straight-line failure interaction locus (Ref 5). The Ni-Cr alloy of this study is generically somewhat similar to stainless steel 304, which is sometimes used as a tool material for high temperature (900 °C) SPF-related processes. Consequently, Shang (Ref 5) has proposed a bilinear creep-fatigue interaction approach for the present XN40F tool material.

Shang (Ref 5) has shown, from FE modeling similar to that of this study, that SPF experience both $\Delta\varepsilon_{\mathrm{pp}}$ and $\Delta\varepsilon_{\mathrm{pc}}$ cyclic inelastic strain ranges, i.e., cyclic strain ranges with plastic strain reversed by plastic strain ($\Delta\varepsilon_{\mathrm{pp}}$) and cyclic strain ranges with plastic strain reversed by creep strain plastic ($\Delta\varepsilon_{\mathrm{pc}}$). Associated with these are two damage components, $D_{\mathrm{pc}} = \frac{N_{\mathrm{f}}}{N_{\mathrm{pc}}}$ and $D_{\mathrm{pp}} = \frac{N_{\mathrm{f}}}{N_{\mathrm{pp}}}$. The bilinear damage summation equations, as shown in Fig. 8(a), are as follows:

$$\frac{N_{\mathrm{f}}}{N_{\mathrm{pp}}} + \beta\frac{N_{\mathrm{f}}}{N_{\mathrm{pc}}} = 1 \quad \text{for } \frac{N_{\mathrm{f}}}{N_{\mathrm{pc}}} < \frac{N_{\mathrm{f}}}{N_{\mathrm{pp}}} \tag{Eq 16}$$

$$\alpha\frac{N_{\mathrm{f}}}{N_{\mathrm{pp}}} + \frac{N_{\mathrm{f}}}{N_{\mathrm{pc}}} = 1 \quad \text{for } \frac{N_{\mathrm{f}}}{N_{\mathrm{pp}}} < \frac{N_{\mathrm{f}}}{N_{\mathrm{pc}}} \tag{Eq 17}$$

where N_{pp} is the number of cycles of $\Delta\varepsilon_{\mathrm{pp}}$ to failure, N_{pc} is the number of cycles of $\Delta\varepsilon_{\mathrm{pc}}$ to failure, and α and β are constants, both greater than 1.

These equations can be further expanded using Miner's rule to linearly combine major and minor cycle damage, as follows:

$$N_{\mathrm{f}}\left[\left(\frac{1}{N_{\mathrm{pp}}^{\mathrm{maj}}} + \frac{2n}{N_{\mathrm{pp}}^{\mathrm{min}}}\right) + \beta\left(\frac{1}{N_{\mathrm{pc}}^{\mathrm{maj}}} + \frac{n}{N_{\mathrm{pc}}^{\mathrm{min}}}\right)\right] = 1 \tag{Eq 18}$$

$$N_{\mathrm{f}}\left[\alpha\left(\frac{1}{N_{\mathrm{pp}}^{\mathrm{maj}}} + \frac{2n}{N_{\mathrm{pp}}^{\mathrm{min}}}\right) + \left(\frac{1}{N_{\mathrm{pc}}^{\mathrm{maj}}} + \frac{n}{N_{\mathrm{pc}}^{\mathrm{min}}}\right)\right] = 1 \tag{Eq 19}$$

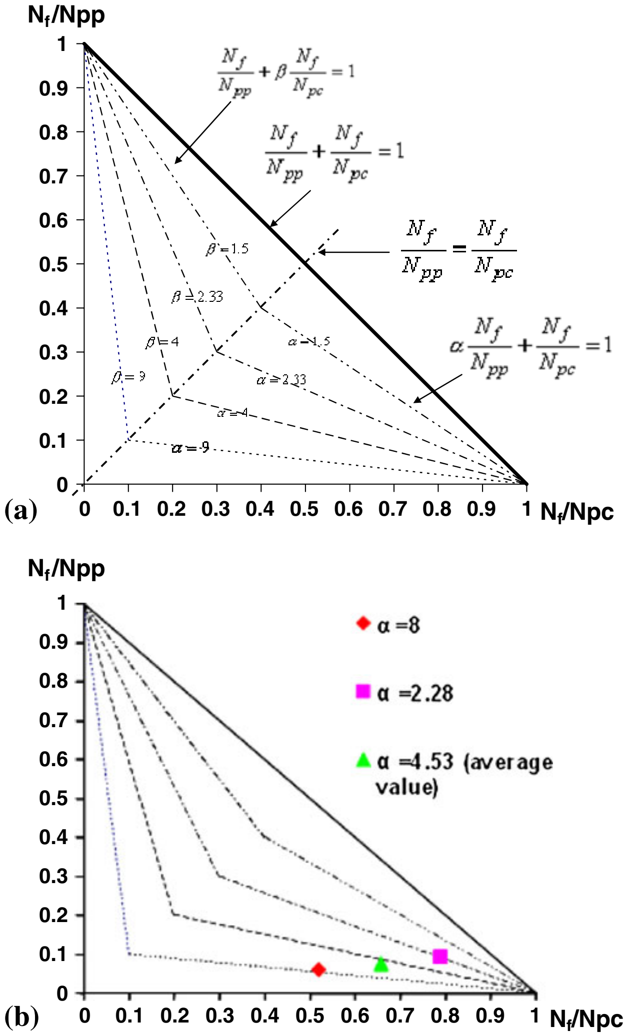

Fig. 8 Bilinear strain range partitioning: (a) schematic plot of the bi-linear damage assumption approach and (b) measured α values from combined creep-fatigue tests on the schematic creep-fatigue interaction diagram (Ref 5)

where n is the number of minor cycles in a major cycle. A typical value of $n = 20$, which is representative of industrial practice for the present application, is considered here for predicting the number of major cycles. The total number of minor cycles is $2n$ to take into account the fact that the press doors are opened and closed separately for blank sheet loading and part unloading operations.

Strain controlled fatigue and fatigue-creep interaction tests on XN40F material were carried out at 700 and 900 °C by Shang (Ref 5) and the resulting cyclic strain-life equations at 900 °C are employed here in the bilinear strain-range partitioning approach, as follows:

$$N_{\mathrm{pp}}(\Delta\varepsilon_{\mathrm{pp}})^{1.346} = 1.745 \tag{Eq 20}$$

$$N_{\mathrm{pc}}(\Delta\varepsilon_{\mathrm{pc}})^{1.518} = 0.462 \tag{Eq 21}$$

Additional tests at 900 °C, specially devised to simulate the interaction between $\Delta\varepsilon_{\mathrm{pp}}$ and $\Delta\varepsilon_{\mathrm{pc}}$ strain ranges for the tool, were employed by Shang (Ref 5), to show that $\frac{N_{\mathrm{f}}}{N_{\mathrm{pp}}} < \frac{N_{\mathrm{f}}}{N_{\mathrm{pc}}}$ for the tool material and to identify the relevant value of α for Eq 17, as shown in Fig. 8(b). The resulting average value of $\alpha = 4.53$ is employed here.

As shown in the Sect 4, the SPF tool exhibits a ratchetting phenomenon, in addition to the creep-fatigue cyclic behavior addressed via the latter bilinear strain-range partitioning approach. The significance of this ratchetting behavior is assessed here via a simple life (crack initiation) prediction approach, based on the study of Kapoor (Ref 7), whereby failure is assumed to occur when the accumulated strain due to ratchetting reaches the uniaxial failure strain (ductility), i.e., a ductility exhaustion approach. Thus, the predicted number of cycles to ratchetting failure, N_r^f, defined here as the occurrence of ductility exhaustion over a volume of approximately 25 mm (typical element size at ratchetting location, with one integration point per element) is given by:

$$N_r^f = \left(\frac{\varepsilon_f}{n\Delta\varepsilon_{eq}^r}\right) \qquad \text{(Eq 22)}$$

where ε_f is the ductility, as determined from tensile tests, and $\Delta\varepsilon_{eq}^r$ is an equivalent ratchet strain, defined as in a manner akin to the definition of equivalent plastic strain, as follows:

$$\Delta\varepsilon_{eq}^r = \left(\sqrt{\frac{2}{3}\left(\Delta\varepsilon_{ij}^r\Delta\varepsilon_{ij}^r\right)}\right) \qquad \text{(Eq 23)}$$

where $\Delta\varepsilon_{ij}^r$ are the tensorial ratchet strain components, calculated from the time histories of each individual strain component, as follows:

$$\Delta\varepsilon_{ij}^r(k) = \varepsilon_{ij}^{in,m}(k) - \varepsilon_{ij}^{in,m}(k-1) \qquad \text{(Eq 24)}$$

where $\varepsilon_{ij}^{in,m}(k)$ is the mean inelastic strain corresponding to the kth minor cycle since, as shown below; the ratchetting phenomenon is associated with the minor cycle creep-plastic deformation. Equation 23 is applied to each minor cycle to obtain a $\Delta\varepsilon_{eq}^r$ value for each minor cycle and an average $\Delta\varepsilon_{eq}^r$ value over all of minor cycles is then employed in Eq 22.

4. Results

4.1 Thermal Results

Figure 9(a) shows the effect of opening and closing of the press doors on the temperature distribution in the tool. Clearly, a significant thermal gradient develops between points adjacent to the front and back doors, e.g., EL C in Fig. 9(a), and points away from the doors, e.g., EL D in Fig. 9(a). Figure 9(b) shows the FE-predicted temperature histories of EL C and EL D, illustrating in particular the significant thermal gradient of

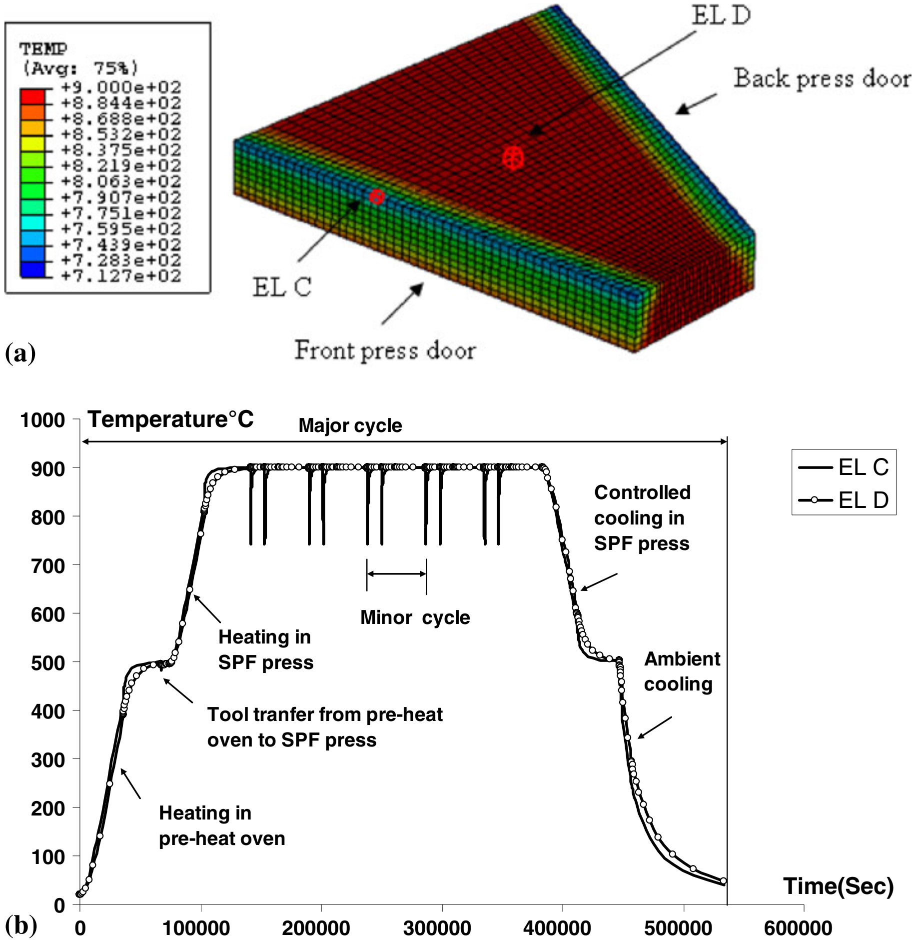

Fig. 9 (a) FE-predicted temperature contour plot at the end of part loading and unloading (minor cycle) and (b) temperature histories for sample elements, EL C and EL D

approximately 150 °C during the opening of the press doors (for five minor cycles). The major cycle heating is controlled according to recommendations from SPF tool manufacturers to a maximum rate of 50 °C/h, which the present and previous analyses, e.g., Ref 5, show as satisfactory with respect to prevent plasticity occurring. Previous study by the authors (Ref 10) has similarly shown that controlled cooling to 500 °C prevents plasticity, as compared to free cooling to ambient from 900 °C. These controls are, therefore, employed in the SPF process. However, control of the minor cycle heating and cooling rates (or indeed time periods) is unfortunately not so readily achievable.

4.2 Thermo-Mechanical Results

4.2.1 Monotonic Material Data. Figure 10 shows the FE-predicted accumulated equivalent plastic strain at the end of three major cycles, each including five minor cycles. Clearly, plasticity is predicted to occur along the top interface edges of the two sides of the tool facing the press doors. As shown in Fig. 9, the temperature drops along these edges during part loading and unloading, leading to large temperature gradients. A local co-ordinate system is defined in Fig. 10 where the *X* direction (also referred to as 1 direction) is parallel to the edge of the tool on which EL C is present and the *Y*-direction (also referred to as 2-direction) is parallel to the thickness of the tool. Figure 11 shows the predicted von-Mises stress history during the first major cycle for EL C. The predicted maximum von Mises stress of 118 MPa occurs during the part loading and unloading operation, when the temperature drops down to 744 °C along the top interface edges of the two sides of the tool facing the press doors, leading to plasticity deformation, as shown in Fig. 12(a), due to the thermal stresses exceeding the temperature-dependent yield stress. In fact, the plastic deformation occurs while the temperature is dropping to 744 °C. The von Mises stress is seen to relax from 107 to 8 MPa during the dwell time at 900 °C, due to creep deformation. The constant clamping pressure of 4 MPa across the edges of the top four sides of the tool is also introduced during the dwell time at 900 °C.

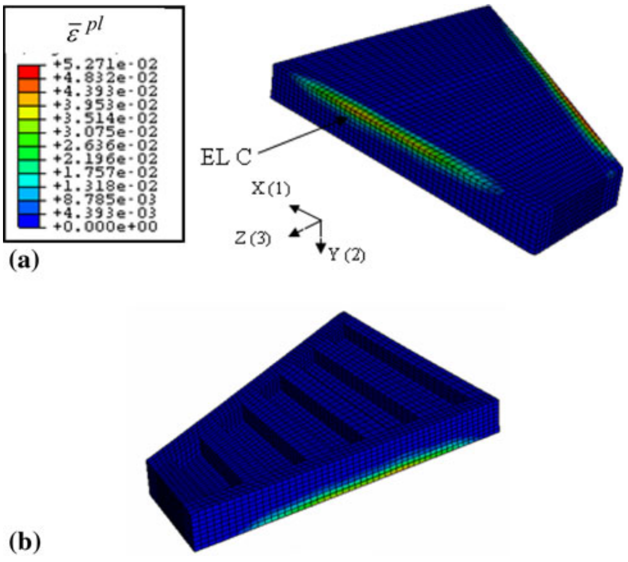

Fig. 10 Equivalent plastic strain distribution at end of third major cycle (monotonic material data) for (a) overhead view of the tool and (b) underside view of the tool

Figure 12(a) shows the predicted local σ_{11} stress versus inelastic strain, ε_{11}^{in} for EL C for three major cycles, including the associated minor cycles. Plastic shakedown is predicted to occur for this combination of stress-strain components, which essentially represents the normal stress-inelastic strain response parallel to the side of the long side of the tool. This suggests that low cycle fatigue is a likely failure mode in this direction.

In order to understand the minor cycle, anisothermal stress-strain response, the local stress-strain response is plotted for the first minor cycle of the first major cycle in Fig. 12(b), for EL C. Thus, this point is predicted to experience compressive stresses during the heating-up process to 900 °C, because it is on the surface and heats up faster than the rest of the tool. No plasticity is predicted to occur during this period which comprises slow heating up to 500 °C in the pre-heat oven, tool transfer from the preheat oven to the SPF press and slow heating up to 900 °C in the SPF press. During tool transfer from the pre-heat oven to the SPF press, tensile stress is predicted due to the bottom surface cooling faster than the top surface, which is modeled as being in contact with the upper half of the tool (via an adiabatic boundary condition).

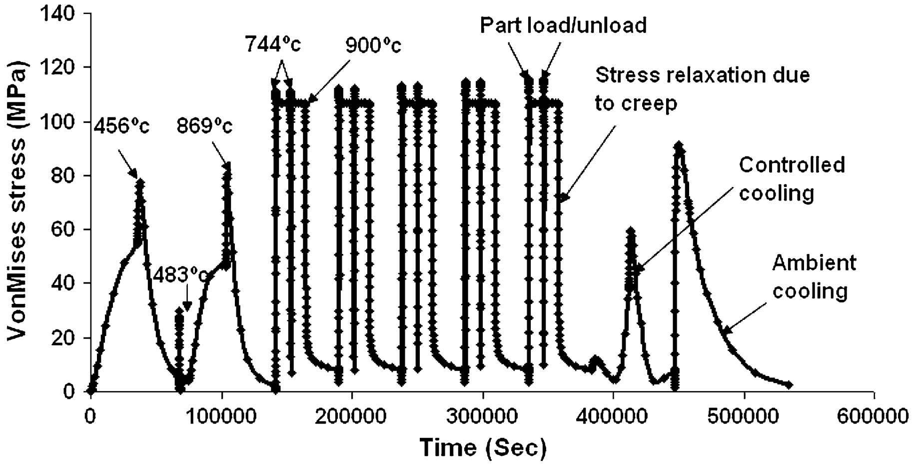

Fig. 11 Predicted von Mises stress history for the first major cycle which includes five minor cycles with monotonic material data

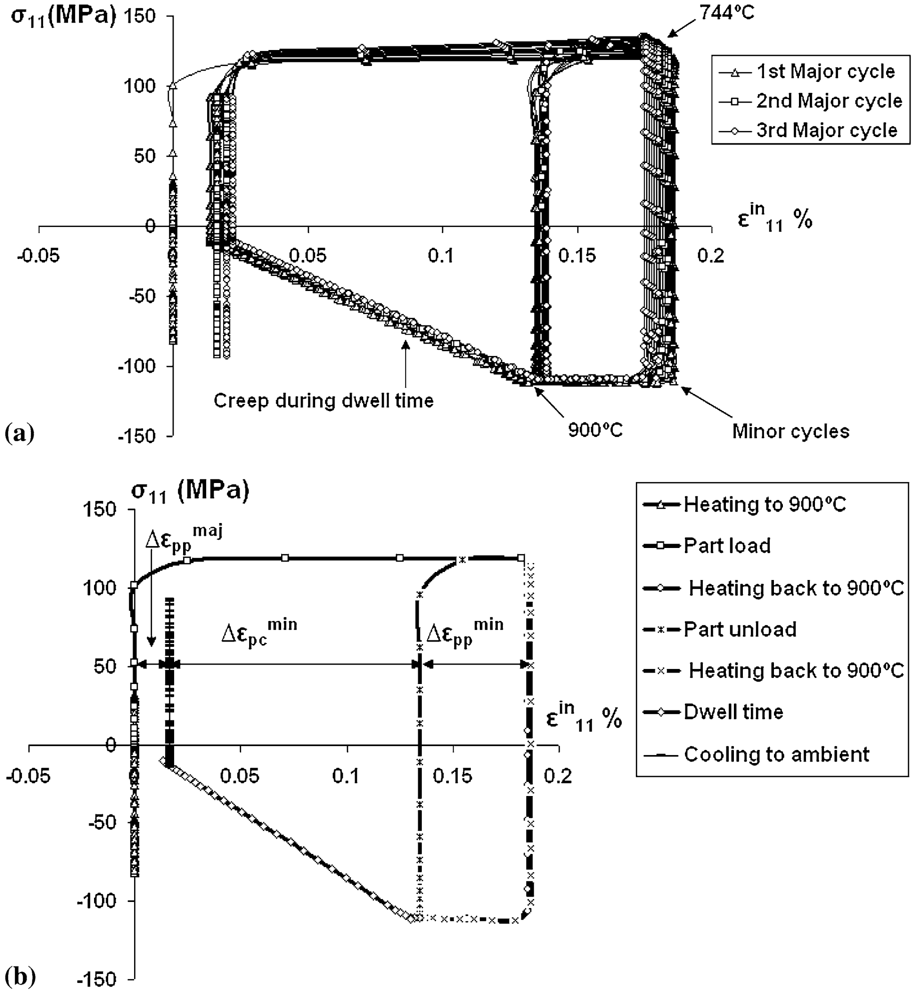

Fig. 12 Local stress vs. local inelastic strain (a) for three major cycles each including five minor cycles with monotonic material data; (b) for the first minor cycle of the first major cycle with monotonic material data

During part loading and unloading, a tensile stress is predicted due to the temperature dropping to 744 °C, the bulk of the tool (i.e., away from the doors) remaining at 900 °C. Elastic recovery followed by compressive plastic strain is predicted during re-heat back to 900 °C after every (minor cycle) part load and unload operation. Compressive creep is predicted to follow the compressive plasticity during the dwell time while the stress relaxation is predicted due to creep. Hence, the analyses predict low cycle fatigue and fatigue-creep interaction damage. Figure 12(b) also shows the inelastic strain ranges $\Delta\varepsilon_{pp}^{maj}$, $\Delta\varepsilon_{pp}^{min}$ and $\Delta\varepsilon_{pc}^{min}$.

In addition to the cyclic plasticity and plasticity reversed by creep cycles, a progressive ratchetting phenomenon is also predicted along the top edges of the tool. This phenomenon results from the fact that the creep strain accrued during the dwell time of the minor cycles exceeds the plastic deformation accrued (due to thermal gradients) during the part loading and unloading processes. This phenomenon is illustrated via the results of Fig. 13 and 14, for EL C. Figure 13(a) shows the predicted evolutions of local inelastic strains, ε_{22}^{in} and ε_{33}^{in}, corresponding to the *Y* and *Z* directions (see Fig. 10 for axes definition) with time, including three major cycles, each with five minor cycles, while Fig. 13(b) shows the corresponding temperature-strain responses. These plots clearly illustrate the progressive strain accumulation. Tensile ratchetting strain is predicted for the *Z*-direction while compressive ratchetting strain is predicted for the *Y*-direction (vertical), leading to an effectively shear-driven ratchetting process (the local strain components correspond to principal strain directions), where the shear is approximately transverse to the *X*-direction and the shear strain is approximately equal in magnitude to the average of ε_{22}^{in} and ε_{33}^{in}. Figure 13(b) shows that the predicted ratchetting is restricted to the approximate temperature range of 744-900 °C. Figure 14 shows the evolution of the mean local inelastic strains, $\varepsilon_{22,m}^{in}$ and $\varepsilon_{33,m}^{in}$, with number of minor cycles, for an analysis of a major cycle which includes 40 minor cycles. Tensile incremental growth is predicted in the *Z*-direction with approximately 0.5% inelastic strain accumulated over the 40 minor cycles, while compressive incremental deformation is predicted in the *Y*-direction with approximately 0.58% inelastic strain accumulated over the 40 minor cycles. No ratchetting is predicted in the *X*-direction.

4.2.2 Cyclic Material Data. Figures 15-18 show the corresponding results from the corresponding analyses using the cyclic material data. It should be pointed out that the material testing indicated that, in general, only about 10-20 cycles were required for cyclic stress-strain stabilization. Attention is focussed again on EL C, which is the predicted

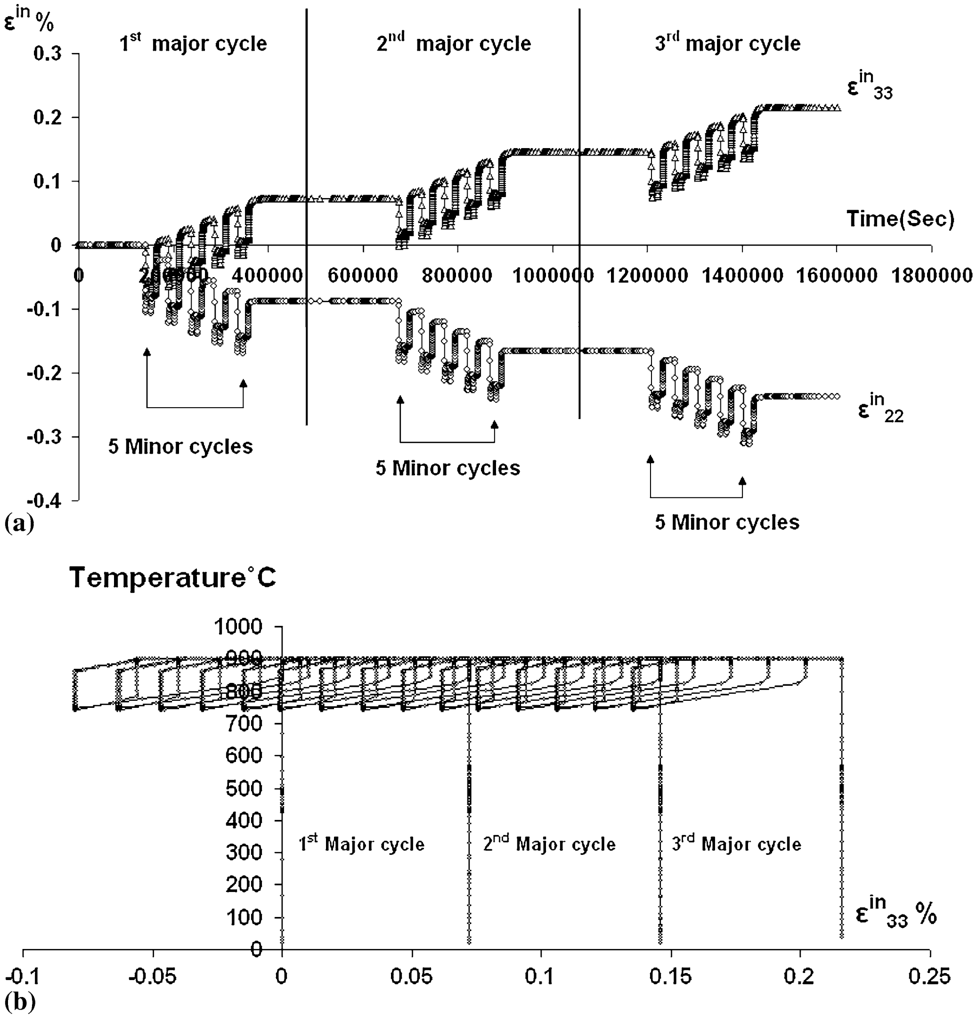

Fig. 13 (a) Predicted time histories of local inelastic strains (ε^{in}_{22} and ε^{in}_{33}) and (b) Temperature vs. ε^{in}_{33} local inelastic strain, over the duration of three major cycles, each including five minor cycles (monotonic material data)

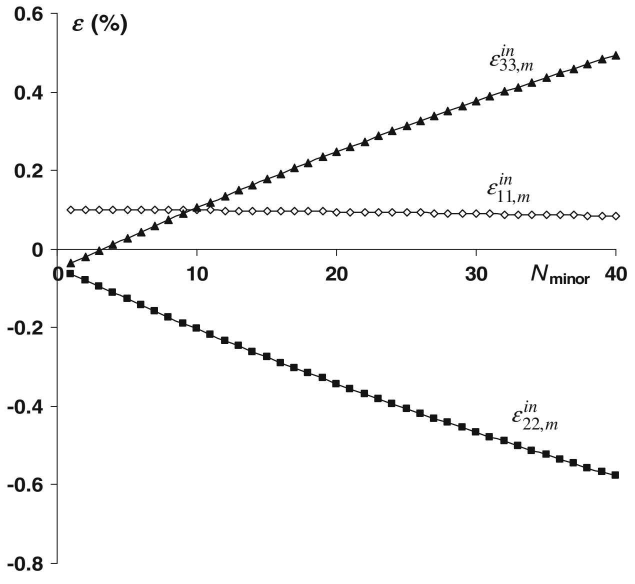

Fig. 14 Predicted evolution of inelastic mean strain with minor cycles (monotonic material data) over one major cycle with 40 minor cycles

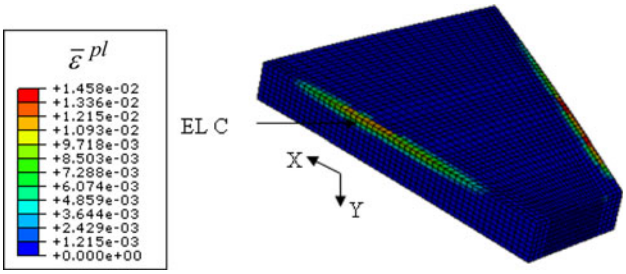

Fig. 15 Equivalent plastic strain distribution at end of third major cycle with cyclic material data

critical location again, as shown in Fig. 15. Figure 16 shows that the von Mises stress history for the first major cycle is akin to that with the monotonic data; one key difference is that the predicted peak stresses are higher than for the monotonic case due to the cyclic hardening behavior of the material. Figure 17(a) shows the predicted local σ_{11}- ε^{in}_{11} response, for three major cycles, each including five minor cycles. In comparison with Fig. 12 (monotonic case), and apparently due to the cyclic hardening slopes being significantly higher than the monotonic values, there is a progressive hardening of the

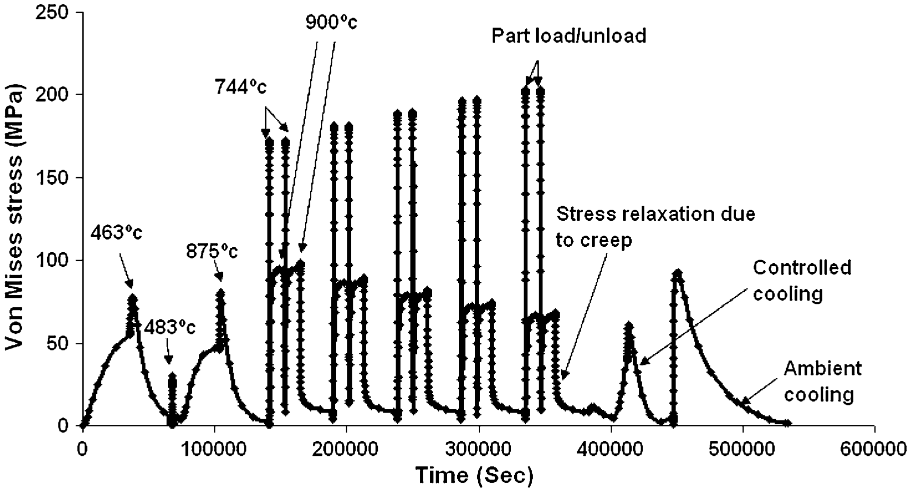

Fig. 16 Predicted von Mises stress history for the first major cycle which includes five minor cycles with cyclic material data

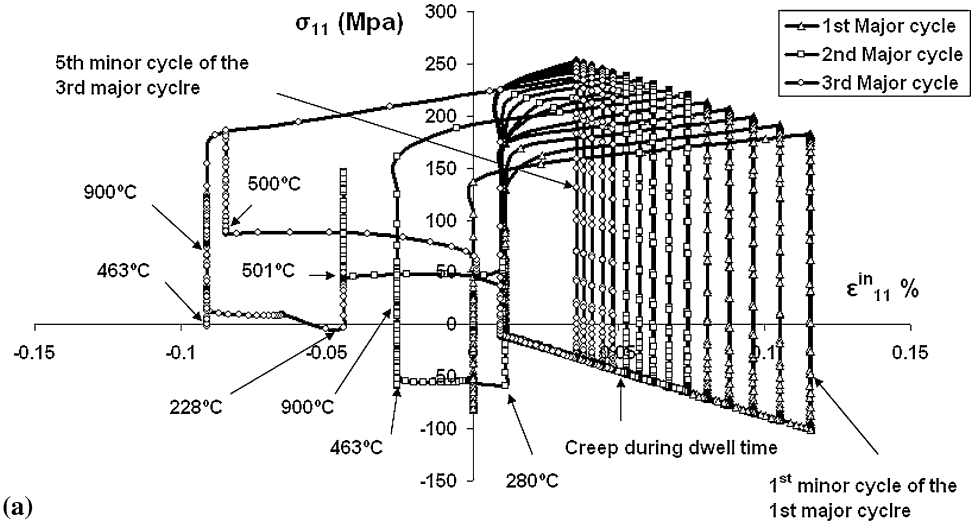

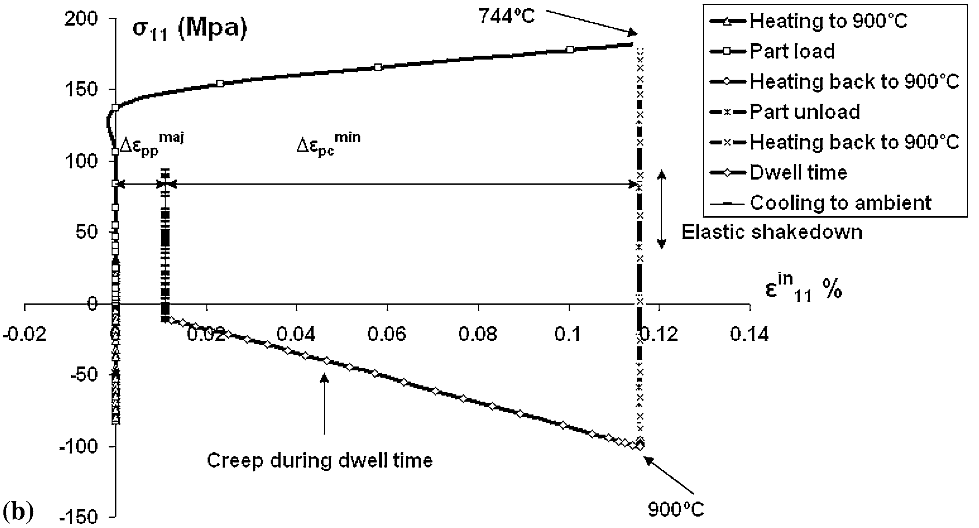

Fig. 17 Local stress vs. local inelastic strain (with cyclic material data): (a) for the first minor cycle of the first major cycle; (b) for the first minor cycle of the first major cycle

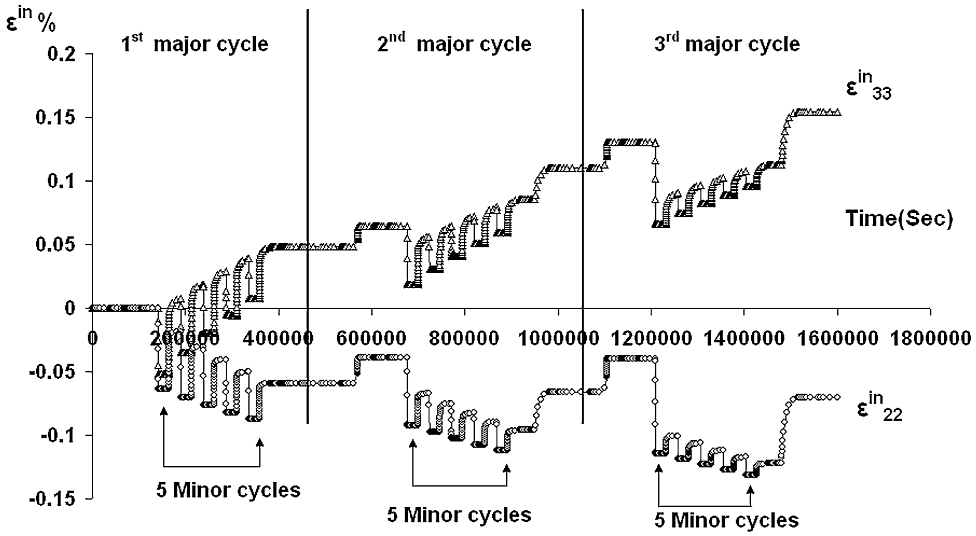

Fig. 18 Local inelastic strains (ε^{in}_{22} and ε^{in}_{33}) history for three major cycles each including five minor cycles (cyclic material data)

material from minor cycle to minor cycle, and from major cycle to major cycle, leading to an increasing mean tensile σ_{11} stress. Figure 17(b) shows the predicted local σ_{11}- ε^{in}_{11} loop for one major cycle (including only one minor cycle) and, in particular, illustrates that elastic shakedown is predicted after the part load operation as the maximum stress predicted during heating back to 900 °C and the subsequent part unload operation is lower than the temperature-dependent yield stress. This will also contribute to the cyclic hardening behavior of Fig. 16(a), since there will be no Bauschinger effect to kinematically shift the yield surfaces back in the compressive direction if compressive yield does not occur. This is almost the reverse of the phenomenon of mean stress relaxation: the mean σ_{11} stress is increasing. The $\Delta\varepsilon^{min}_{pp}$minor cycle strain range is thus zero. Figure 18 shows the predicted evolutions of local inelastic strains, ε^{in}_{22} and ε^{in}_{33} with time, including three major cycles, each with five minor cycles. Again, the trends are akin to those of the monotonic data case, except that the magnitude of the strain accumulation is less, due to the cyclic hardening effects. Figure 19 shows the predicted evolutions of mean inelastic strains with minor cycles for the cyclic data case for a major cycle analysis with 40 minor cycles. Although the general trends are similar to the monotonic data case (cf. Fig. 14), the key differences are (i) that the total accumulated strains are lower, and (ii) the rates of ratchetting are decreasing at a faster rate. This phenomenon is called finite ratchetting (Ref 11). Plastic shakedown is predicted to occur after initial finite ratchetting in the *X*-direction. In contrast to the monotonic results, Fig. 17(a) shows that compressive plastic strain is predicted to occur during the second and third major cycles, during heating in the pre-heat oven (from 280 to 463 °C) and during controlled cooling from 900 to 501 °C (see Fig. 17a).

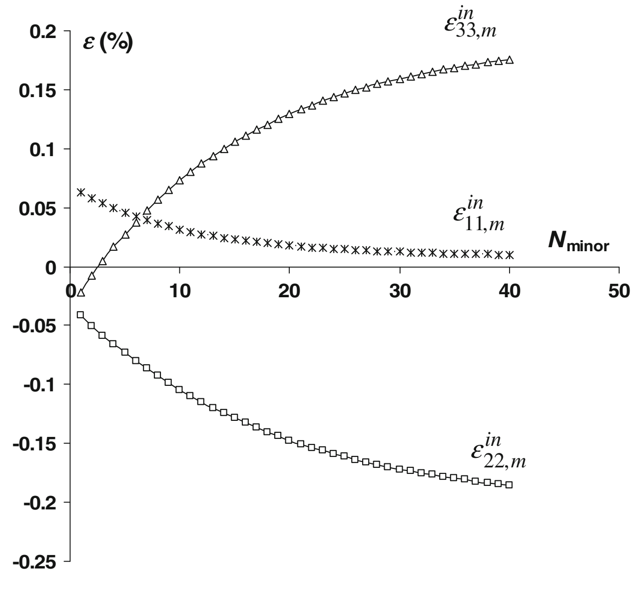

Fig. 19 Local inelastic mean strains vs. number of minor cycles (cyclic material data)

Table 6 Predicted fatigue-creep life (major cycles) with bi-linear strain range partitioning approach

	Monotonic data	Cyclic data
$\alpha = 4.53$	178	765

Table 7 Predicted ratchetting lives, N^f_r

Parameter	Monotonic data	Cyclic data
$\Delta\varepsilon^{eq}_r$ average	0.015%	0.0044%
ε_f at 900 °C	123	420
ε_f at 700 °C	53	182

4.3 Tool Life Predictions

Tables 6 and 7 summarize the creep-fatigue life predictions from the bi-linear strain range partitioning method and the ratchetting crack initiation lives, respectively. For the latter, since the ratchetting is accumulated between about 740 and 900 °C, it is not clear which temperature the isothermal ductility data should correspond to. Furthermore, each major cycle is assumed to have 20 minor cycles, corresponding to 20 formed parts per forming campaign, which is typical of industrial practice for the present tool, based partly on recent findings by Deshpande et al. (Ref 10). Clearly, increasing the number of parts formed per campaign, will proportionally reduce the predicted number of major cycles to ratchetting crack initiation and have a similar effect on creep-fatigue life. The predicted creep-fatigue life using the cyclic data is much higher than using the monotonic data, mainly due to the elastic shakedown predicted during part unload and heating back to 900 °C for the cyclic data case. The average equivalent ratchet strain $\Delta\varepsilon_r^{eq}$ over 40 minor cycles (cf. Fig. 14 and 19) is considered for the ratchet life prediction.

5. Discussion

The life-limiting phenomena such as ratchetting and fatigue due to cyclic loading generally occur simultaneously in the low cycle fatigue regime. This article has shown that creep-plastic ratchetting is predicted to occur also in SPF tools under realistic thermal and mechanical loading histories, in addition to the previously presented (predicted) phenomenon of creep-fatigue damage. These phenomena are considered to be independent here, and the SPF tool life is predicted separately based on these individual mechanisms. A number of assumptions were made which can be improved upon in future study, as follows:

- A realistic but idealized thermal and mechanical loading history for industrial SPF tools is modeled here. Further study should examine the effects of variations in key variables, such as duration for loading and unloading the forming medium, more complex variations (temporal and spatial) in clamping load, incorporation of the effects of the forming cycle proper, the effect of the upper tool, platen deformation effects etc. A simplified SPF tool is modeled and complex geometry features such as alignment lugs, forming surface corners, and hangers are excluded. Clearly, these could be expected to have a significant effect on predicted life, particularly if located at the co-location of creep-fatigue damage and ratchetting damage.
- The predicted ratchetting phenomenon is predicted in the plane transverse to the predominant creep-fatigue direction. Consequently, some type of multiaxial interaction is likely. Thus, the ratchetting process may accelerate damage accumulation by void growth, for example, and this may further exacerbate the creep-fatigue process, leading to significantly shorter lives even than those predicted.
- Although the material model employed was temperature dependent and incorporated rate-independent plasticity with kinematic-hardening effects and uncoupled creep, more complex material models are available, e.g., unified cyclic viscoplasticity models with combined non-linear kinematic hardening and isotropic hardening, so that cyclic stabilization can also be modeled. The attraction of the present process is the ease with which the required material constants can be obtained.

The predicted SPF tool behavior and predicted tool life are consistent with industrial observations. Thus, for example, since most XN40F tools are used for less than about 100 major cycles, cracking is not generally a problem, but there have been notable and costly exceptions to this; also, this study is more generally concerned with the development of pragmatic lifing methodologies for advising industrial practice with respect to the tool operation. However, the tool refurbishment is a continual problem, with persistent interruptions to tool and press operation required for re-machining to maintain tolerances on formed parts. The immediate onset of progressive deformation, see also Ref 10, shows how this can occur.

6. Conclusion

A FE methodology for predicting the cyclic thermomechanical behavior of a representative large SPF tool under simplified but realistic thermal and mechanical loading histories is studied. The high temperature (isothermal) monotonic and cyclic stress-strain behavior of the tool material, XN40F, is presented. Some key conclusions from the study are as follows:

- Plastic strain is predicted along the exposed sides (top edges) of the tool during opening of the press. This strain is predominantly in the direction parallel to these sides.
- Ratchetting is predicted at the same general locations of the tools, i.e., top edges of exposed sides during press opening, but the ratchetting direction is in the transverse plane to the exposed sides.
- Crack initiation predictions for the ratchetting phenomenon, based on uniaxial ductility exhaustion, give shorter lives than the creep-fatigue prediction methodology, which is based on a bi-linear strain-range partitioning method to combine creep and fatigue damage.
- It is shown that using monotonic data instead of cyclic data predicts shorter creep-fatigue and ratchetting lives, due to cyclic hardening of the tool material. Predicted lives ranged between approximately 50 and 1000 cycles. These are broadly consistent with industrial tool performance.

Acknowledgments

The authors wish to thank Ian Leaver and John Chippendale of BAE Systems, Salmesbury for helpful discussions. The first author would also like to thank BAE Systems for funding.

References

1. G. Bernhart, F. Nazaret, A. Martinier, C. Gao, D. Garriga-Majo, T. Cutard, and P. Lours, Design of SPF Dies Based on Advanced Material Behaviour Models, *Mater. Sci. Forum*, 2004, **447–448**, p 123–130
2. C.Y. Gao, P. Lours, and G. Bernhart, Thermomechanical Stress Analysis of Superplastic Forming Tools, *J. Mater. Process. Technol.*, 2005, **169**, p 281–291
3. J. Shang, S.B. Leen, and T.H. Hyde, Finite Element Based Methodology for Predicting the Thermomechanical Behaviour of Superplastic Forming Tools, *Proc. IMechE, Part L: J. Mater.: Des. Appl.*, 2006, **220**(L3), p 113–123
4. J. Shang, S.B. Leen, and T.H. Hyde, Finite Element Based Life Prediction for High Temperature Cyclic Loading of a Large Superplastic Forming Die, *J. Strain Anal.*, 2006, **41**(8), p 539–559
5. J. Shang, "Thermo-Mechanical Life Assessment of Superplastic Forming Tools," Ph.D. thesis, University of Nottingham, September 2005

6. G. Kang and Q. Kan, Constitutive Modelling for Uniaxial Time-Dependent Ratchetting of SS304 Stainless Steel, *Mech. Mater.*, 2007, **39**(5), p 488–499
7. A. Kapoor, A Re-Evaluation of the Life to Rupture of Ductile Metals by Cyclic Plastic Strain, *Fatigue Fract. Eng. Mater. Struct.*, 1994, **17**(2), p 201–219
8. A. Bejan, *Heat Transfer*, John Wiley and Sons, 1993
9. *ABAQUS User and Theory Manuals, Version 6.5*, HKS Inc., Rhode Island, US, 2004
10. A.A. Deshpande, S.B. Leen, and T.H. Hyde, Finite Element Based Predictions of Life Limiting Behaviour for a Large SPF Tool, *Materwiss. Werksttech.*, 2008, **39**(4–5), p 309–316
11. H. Hübel, Basic Conditions for Material and Structural Ratchetting, *Nucl. Eng. Des.*, 1996, **162**(1), p 55–65